

SCIENTIFIC REPORTS

OPEN

Investigation of AlGa_xN/GaN high electron mobility transistor structures on 200-mm silicon (111) substrates employing different buffer layer configurations

H.-P. Lee^{1,2}, J. Perozek^{1,2}, L. D. Rosario^{1,2} & C. Bayram^{1,2}

Received: 23 August 2016
Accepted: 31 October 2016
Published: 21 November 2016

AlGa_xN/GaN high electron mobility transistor (HEMT) structures are grown on 200-mm diameter Si(111) substrates by using three different buffer layer configurations: (a) Thick-GaN/3 × {Al_xGa_{1-x}N}/AlN, (b) Thin-GaN/3 × {Al_xGa_{1-x}N}/AlN, and (c) Thin-GaN/AlN, so as to have crack-free and low-bow (<50 μm) wafer. Scanning electron microscopy, energy-dispersive X-ray spectroscopy, high resolution-cross section transmission electron microscopy, optical microscopy, atomic-force microscopy, cathodoluminescence, Raman spectroscopy, X-ray diffraction ($\omega/2\theta$ scan and symmetric/asymmetric ω scan (rocking curve scan), reciprocal space mapping) and Hall effect measurements are employed to study the structural, optical, and electrical properties of these AlGa_xN/GaN HEMT structures. The effects of buffer layer stacks (i.e. thickness and content) on defectivity, stress, and two-dimensional electron gas (2DEG) mobility and 2DEG concentration are reported. It is shown that 2DEG characteristics are heavily affected by the employed buffer layers between AlGa_xN/GaN HEMT structures and Si(111) substrates. Particularly, we report that in-plane stress in the GaN layer affects the 2DEG mobility and 2DEG carrier concentration significantly. Buffer layer engineering is shown to be essential for achieving high 2DEG mobility (>1800 cm²/V·s) and 2DEG carrier concentration (>1.0 × 10¹³ cm⁻²) on Si(111) substrates.

AlGa_xN/GaN high electron mobility transistors (HEMTs) are being investigated for high power high frequency applications as III-nitride (i.e. GaN) materials have high thermal and chemical stability, high breakdown field (>3 MV/cm, 10 times of that of silicon), and high electron saturation velocity (>2.5 × 10⁷ cm/s, 2.5 times of that of silicon)¹⁻³. AlGa_xN/GaN HEMTs are traditionally grown on sapphire (Al₂O₃) or silicon carbide (6H-SiC) substrates that have ~16% and ~3% lattice-mismatch with GaN, respectively⁴. Recently, high cost and limited diameter-scalability of these substrates fueled the research for the GaN-on-silicon (111) approach⁵. However, the lattice mismatch of ~17% combined with the thermal-expansion-coefficient mismatch of ~54% between GaN and Si(111) necessitate employment of novel (Al)GaN buffer layers to minimize mismatch-effects (i.e. defectivity and wafer-bow)⁶. It is reported that several micrometer thick buffer layers and various Al-content Al_xGa_{1-x}N layers are needed to mitigate such detrimental effects of lattice and thermal-mismatches⁷. Nonetheless, performance of AlGa_xN/GaN HEMTs is governed by the two-dimensional electron gas (2DEG) properties, which forms at the AlGa_xN-GaN hetero-interface and without the need of any doping – thanks to the high conduction band offset and polarization fields between AlGa_xN and GaN⁸. Particularly, a high 2DEG density reduces the source/drain contact resistance⁹ and increases the power output of AlGa_xN/GaN HEMTs³ whereas high 2DEG mobility increases the frequency performance of AlGa_xN/GaN HEMTs¹⁰. It is therefore imperative to study the characteristics of the 2DEG and investigate how 2DEG characteristics change under various buffer layer configurations. To do so, the same AlGa_xN/GaN HEMT structures need to be grown on Si(111) but with various buffer layers⁷.

¹Department of Electrical and Computer Engineering, University of Illinois at Urbana-Champaign, Urbana, Illinois 61801, USA. ²Micro and Nanotechnology Laboratory, University of Illinois at Urbana-Champaign, Urbana, Illinois 61801, USA. Correspondence and requests for materials should be addressed to C.B. (email: cbayram@illinois.edu)

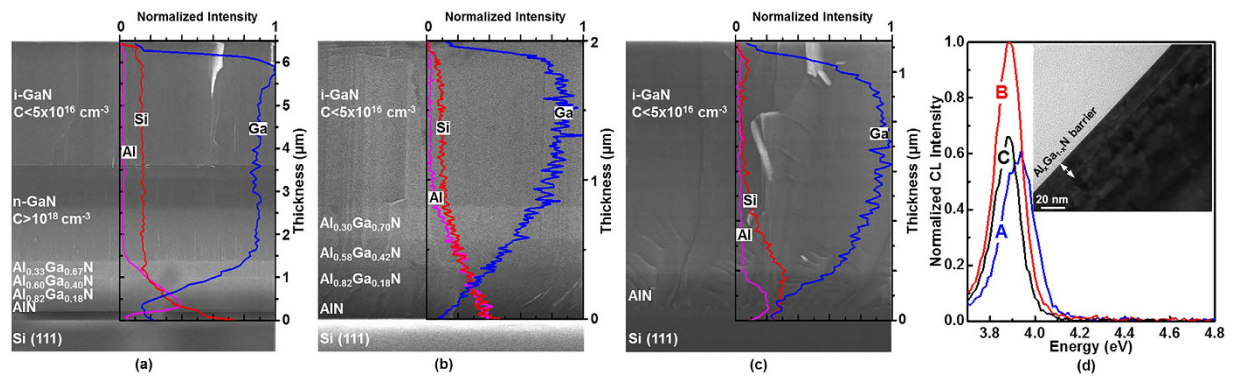


Figure 1. SEM cross section, EDS, HR-XTEM, and CL investigations of the AlGaIn/GaN HEMT structures grown on Si(111) substrate with three different buffer configurations are shown. (a) Thick-GaN/ $3 \times \{\text{Al}_x\text{Ga}_{1-x}\text{N}\}/\text{AlN}$ (Sample A), (b) Thin-GaN/ $3 \times \{\text{Al}_x\text{Ga}_{1-x}\text{N}\}/\text{AlN}$ (Sample B), and (c) Thin-GaN/AlN (Sample C). Atop of all samples (A, B, C), the same AlGaIn/GaN HEMT structure, composed of 2-nm-thick i-GaN/17-nm-thick $\text{Al}_x\text{Ga}_{1-x}\text{N}$ /1-nm-thick AlN, is deposited as shown in (d). Based on the CL spectrum peak position of the $\text{Al}_x\text{Ga}_{1-x}\text{N}$ barrier layer, Al composition can be estimated as 0.25, 0.23, and 0.22 for sample A, B, and C, respectively.

Another important milestone in GaN-on-Si(111) technology is Si(111) wafer-scaling. Despite the early works on 100-mm substrates¹¹, it is critical to scale these efforts to 200-mm substrates. This, however, is bottlenecked primarily by the large GaN-Si thermal mismatch that introduces high stress leading to significant wafer-bow¹² or worse, wafer cracking¹³.

In this work, we grew the same AlGaIn/GaN HEMT structures on 200-mm Si(111) substrates using three different buffer layers configurations {such that all wafers are crack-free and have a small bow ($<50\ \mu\text{m}$)} and report the effects of buffer layers on the AlGaIn/GaN HEMT structures. To quantify the stress and defectivity, we investigate these stacks using structural, optical and electrical characterization techniques including scanning electron microscopy (SEM), energy-dispersive X-ray spectroscopy (EDS), high resolution cross-sectional transmission electron microscopy (HR-XTEM), optical microscopy, atomic-force microscopy (AFM), cathodoluminescence (CL), Raman spectroscopy, X-ray diffraction (XRD) $\{\omega/2\theta$ scan, symmetric/asymmetric ω scan (rocking curve scan), and reciprocal space mapping (RSM)} and Hall effect measurements. Then we correlate the electrical properties of AlGaIn/GaN HEMT structures with the embodied buffer layer properties and report the effects of buffer layer stress and defectivity on the 2DEG mobility and 2DEG concentration.

Results

Investigating the AlGaIn/GaN HEMT structures and the underlying buffer layer configurations.

Figure 1 shows the AlGaIn/GaN HEMT structures grown on Si(111) substrate with three different buffer configurations: (a) Thick-GaN/ $3 \times \{\text{Al}_x\text{Ga}_{1-x}\text{N}\}/\text{AlN}$ (Sample A), (b) Thin-GaN/ $3 \times \{\text{Al}_x\text{Ga}_{1-x}\text{N}\}/\text{AlN}$ (Sample B), and (c) Thin-GaN/AlN (Sample C). Hitachi S-4700/S-4800 high resolution SEM is used to measure layer thicknesses. All three configurations employ an AlN buffer layer (240-nm-thick, 175-nm-thick, and 130-nm-thick in samples A, B, and C, respectively) on top of the Si(111) substrate to prevent Ga-etch back during (Al)GaN growth¹⁴. On top of the AlN buffer layers, samples A and B have three step-graded $\text{Al}_x\text{Ga}_{1-x}\text{N}$ buffer layers (400-nm-thick $\text{Al}_{0.33}\text{Ga}_{0.67}\text{N}$ /290-nm-thick $\text{Al}_{0.60}\text{Ga}_{0.40}\text{N}$ /200-nm-thick $\text{Al}_{0.82}\text{Ga}_{0.18}\text{N}$ in sample A and 240-nm-thick $\text{Al}_{0.30}\text{Ga}_{0.70}\text{N}$ /210-nm-thick $\text{Al}_{0.58}\text{Ga}_{0.42}\text{N}$ /190-nm-thick $\text{Al}_{0.82}\text{Ga}_{0.18}\text{N}$ in sample B) whereas sample C has no AlGaIn buffer layer. Then, 2280-nm-thick n-doped (n-) followed by 2880-nm-thick intrinsic (i-) GaN layers were grown for sample A whereas only 1200- and 950-nm-thick intrinsic GaN layers were deposited on samples B and C, respectively. Atop of all samples, the same AlGaIn/GaN HEMT structure, composed of 2-nm-thick i-GaN/17-nm-thick $\text{Al}_x\text{Ga}_{1-x}\text{N}$ /1-nm-thick AlN, was deposited. Figure 1d shows HR-XTEM and CL of the AlGaIn/GaN HEMT structure. Intrinsic GaN cap protects the $\text{Al}_x\text{Ga}_{1-x}\text{N}$ barrier layer surface and minimizes the electrical contact resistance for Hall measurements¹⁵. To minimize layer relaxation through defect generation at the $\text{Al}_x\text{Ga}_{1-x}\text{N}$ -GaN hetero-interface, only a 17-nm-thick $\text{Al}_x\text{Ga}_{1-x}\text{N}$ barrier layer (measured by HR-XTEM) is grown¹⁶. We also employed CL spectroscopy (JEOL 7000F analytical Schottky field emission SEM equipped with Gatan MonoCL3 CL Spectrometer) to probe the bandgap energy of the $\text{Al}_x\text{Ga}_{1-x}\text{N}$ barrier layer for estimating the Al composition. Cathodoluminescence measurement was conducted with 5x magnification, 1.5 kV electron acceleration voltage (which yields a 29-nm penetration depth based on Kanaya-Okayama formula¹⁷), and 2 nA current. The measured spectrum was fitted using Gaussian distribution and the peak positions were obtained as 3.924 eV, 3.882 eV, and 3.874 eV for sample A, B, and C, respectively. Based on the peak position, we calculated the Al composition (x) of the $\text{Al}_x\text{Ga}_{1-x}\text{N}$ barrier layer to be 0.25, 0.23, and 0.22 for sample A, B, and C, respectively¹⁸. The AlN spacer layer is inserted between the $\text{Al}_x\text{Ga}_{1-x}\text{N}$ barrier and GaN to increase the conduction band offset and the 2DEG confinement in order to increase 2DEG concentration and mobility^{19,20}. Overall, samples A, B, C have the total epilayer thickness of 6.3, 2.0, and 1.2 μm , respectively (Fig. 1).

The critical elemental compositions (i.e. Al, Ga, Si) across these samples (i.e. A, B, C) are investigated by Oxford Instrument ISIS EDS X-ray microanalysis system with a spatial resolution of $\sim 1\ \mu\text{m}$ and plotted in Fig. 1. In samples A and B, from GaN layer towards the Si(111) substrate, the Ga signal decreases as the Al signal

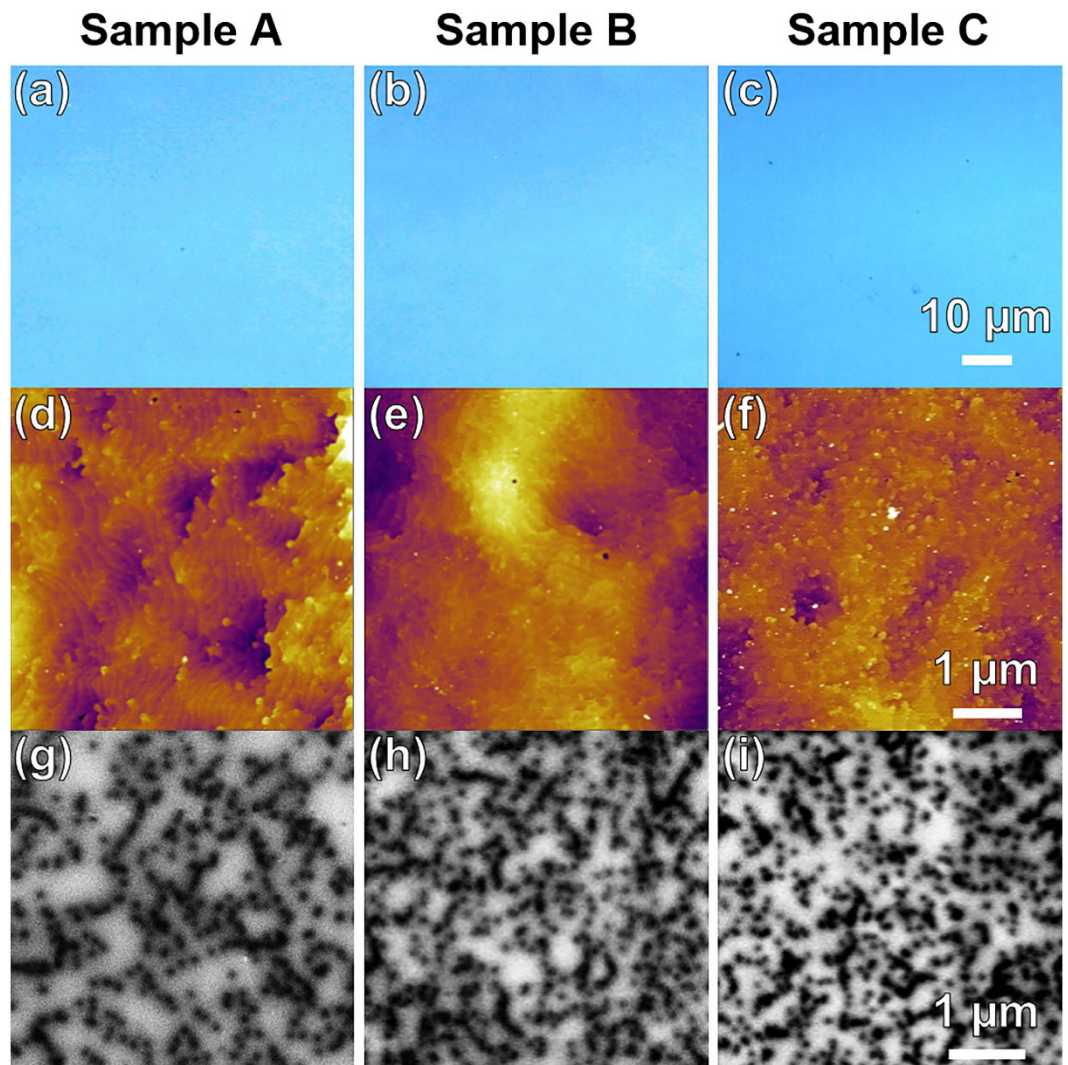


Figure 2. Optical microscopy, AFM and CL images of samples A, B and C are shown. Optical microscopy (a,b,c) reveals no surface cracks. AFM (d,e,f) reveals the average root-mean-square (RMS) roughness of 5.5 ± 2.8 , 5.2 ± 1.4 , and 5.1 ± 1.3 Å for sample A, B, and C, respectively, suggesting a similar surface profile. Cathodoluminescence (g,h,i) reveals defectivity of sample A, B, and C as $1.0 \pm 0.3 \times 10^9$, $2.0 \pm 0.3 \times 10^9$, $1.8 \pm 0.3 \times 10^9$ cm⁻², respectively. AFM and CL studies agree that sample A (the thickest sample) has the lowest threading dislocation defect density whereas sample C (the thinnest sample) has the highest one (Table 1).

increases, as we have step-graded Al_xGa_{1-x}N layers. In sample C a rather rounded Al signal peak is observed as it has no step-graded Al_xGa_{1-x}N layers. The Si signal increases in all samples towards the substrate showing the Si diffusion.

Surface investigation of the AlGaN/GaN HEMT structures via optical microscope, atomic force microscopy, and cathodoluminescence. Figure 2 shows the surface studies of all samples (A, B, C) by optical microscopy (Fig. 2a,b,c), atomic force microscopy (Fig. 2d,e,f) and CL (Fig. 2g,h,i). No surface cracks are observed in any samples, indicating high film quality¹³. Atomic force microscopy (Asylum Cypher S AFM with tapping mode) is used to study the surface roughness and contour of the AlGaN/GaN HEMT structures. Figure 2d,e,f show 5 μm × 5 μm AFM scans. It is important to note that the average root-mean-square (RMS) roughnesses are similar across samples (5.5 ± 2.8 , 5.2 ± 1.4 , and 5.1 ± 1.3 Å, for A, B, and C, respectively), wherein sample A has the largest surface roughness. In order to quantify surface-terminated defects (i.e. dislocations with threading component), we counted the “dark spots” on the AFM images (Fig. 2d,e,f)²¹ which averaged as $1.8 \pm 0.3 \times 10^9$, $2.2 \pm 0.8 \times 10^9$, and $2.6 \pm 0.8 \times 10^9$ cm⁻² (Table 1) for samples A, B, and C, respectively, showing thickest sample (A) having the lowest density of threading type dislocations, in agreement with other works^{22,23}. Based on their different sizes these dark spots can be classified as pure-edge type (small), pure-screw type (large) and mixed-type (middle) threading dislocations.

Cathodoluminescence is also a useful tool in highlighting the surface defects as defects are centers of non-radiative recombination and appear dark in a panchromatic view²⁴. We again employed the same CL

Sample (Epi thickness)	AFM surface roughness (Å)	Defectivity (10^9 cm^{-2})				GaN stress (GPa)			Electrical property					
		AFM	CL	XRD		XRD	Raman	R_s (Ω/\square)		2DEG N_s (10^{13} cm^{-2})		2DEG μ_n ($\text{cm}^2/\text{V}\cdot\text{s}$)		
				D_{screw}	D_{edge}	Tensile	Compressive	RT	77 K	RT	77 K	RT	77 K	
A (6.3 μm)	5.5 ± 2.8	1.8 ± 0.3	1.0 ± 0.3	0.40	1.02	1.059	0.256	431.8 ± 109.8	110.8 ± 28.1	1.20 ± 0.01	1.30 ± 0.10	1295 ± 247	4867 ± 996	
B (2.0 μm)	5.2 ± 1.4	2.2 ± 0.8	2.0 ± 0.3	0.58	1.47	0.154	0.488	385.8 ± 28.1	66.5 ± 5.0	0.89 ± 0.01	1.00 ± 0.01	1802 ± 102	9175 ± 698	
C (1.1 μm)	5.1 ± 1.3	2.6 ± 0.8	1.8 ± 0.3	0.39	1.02	1.548	0.047	445.5 ± 75.3	96.0 ± 23.0	0.92 ± 0.05	1.00 ± 0.10	1593 ± 268	6930 ± 1541	

Table 1. Structural (surface roughness, defectivity, stress) and electrical (contact resistance, 2DEG concentration, 2DEG mobility) properties of samples A, B, and C are tabulated.

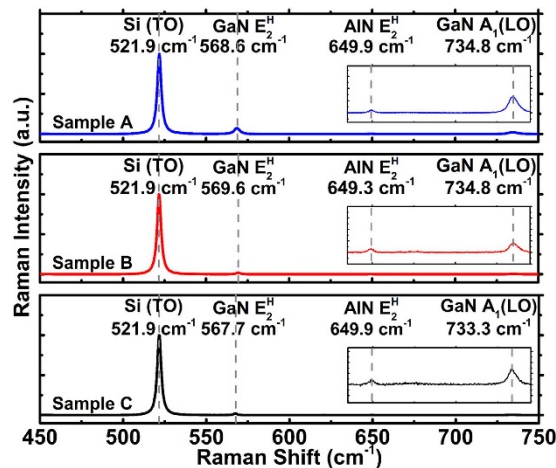


Figure 3. Raman spectroscopy of all samples A, B, and C are shown.

spectroscopy system to study these samples. A panchromatic CL image using a 2.0-kV electron acceleration voltage (that gives a penetration depth of 47 nm¹⁷) reveals the defect distribution as shown in Fig. 2g,h,i. The average CL defectivity for samples A, B, and C are measured as $1.0 \pm 0.3 \times 10^9$, $2.0 \pm 0.3 \times 10^9$, and $1.8 \pm 0.3 \times 10^9 \text{ cm}^{-2}$ (Table 1), respectively. This suggests, similar to our AFM results, that the thickest sample A has the least defectivity. With respect to AFM analysis, CL underestimates the defectivity because defects have capture radius, suggesting that multiple defects are located within one CL dark capture radius.

Layer stress analysis through Raman measurements, X-ray diffraction and reciprocal space mapping.

We studied the GaN stress via Horiba Raman Confocal Imaging Microscope using 633-nm laser line (with a grating of 1800 lines/mm, yielding a resolution of 1.19 cm^{-1}). A 2'' Si(111) wafer was first utilized for spectrum verification and a 521.9 cm^{-1} peak was obtained, as shown in Figure S1. Under $Z(XX)\bar{Z}$ configuration, E_2^H and $A_1(\text{LO})$ Raman peaks are measured, and the shifts in these Raman peaks from the stress-free values of 567.5 cm^{-1} (E_2^H) at 300 K are recorded. Based on the shift direction and the shift amount ($\Delta\omega$) of E_2^H , we determined the stress type as compressive and calculated the stress amount (σ_{xx}) through¹¹

$$\sigma_{xx} = \frac{\Delta\omega}{4.3} \text{ cm} \cdot \text{GPa} \quad (1)$$

and tabulated them in Table 1. The Raman spectra of sample A, B, and C are also plotted in Fig. 3. Our Raman spectroscopy investigation suggests that sample B is under the largest compressive stress (0.488 GPa) whereas sample C is under the smallest compressive stress (0.047 GPa) and sample A has the medium value (0.256 GPa). These results are similar to other Raman works on AlGaIn/GaN HEMT structures on Si(111)¹¹.

We further quantify the (Al)GaN layers' composition, strain, and defect density via XRD^{25,26}. Here we employ PANalytical/Philips X'pert MRD system with 0.154-nm-wavelength radiation to study all samples. Omega/2Theta ($\omega/2\theta$) scan is used to probe the symmetrical lattice plane (0002) to determine the Al compositions of the $\text{Al}_x\text{Ga}_{1-x}\text{N}$ buffer layers according to:

$$x_{\text{Al}} = (c_{\text{Al}_x\text{Ga}_{1-x}\text{N}} - c_{\text{GaN}}) / (c_{\text{AlN}} - c_{\text{GaN}}), \quad (2)$$

where c represents the lattice constant along the c axis calculated via Vegard's law²⁷. Figure 4 shows the $\omega/2\theta$ scans of samples A, B, and C. The narrowest FWHM of sample B indicates the highest crystalline order amongst the samples, whereas sample A has the lowest crystalline order indicated by its widest FWHM. However, one should be aware that the Al composition results obtained from XRD $\omega/2\theta$ scan can be inaccurate since both the epilayer

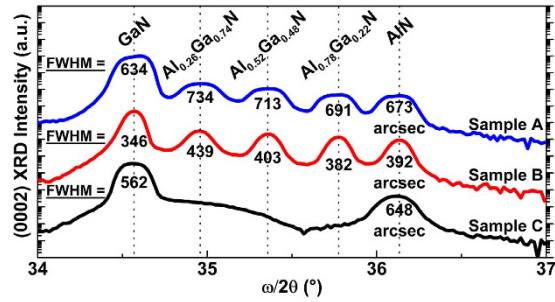


Figure 4. Symmetric XRD $\omega/2\theta$ scans of samples A, B, and C are used to determine the Al-content and crystalline quality. Results show sample B having the narrowest FWHM values – suggesting the best crystallography quality amongst all samples.

strain and alloy composition will significantly affect the peak position of the $\omega/2\theta$ scan; to estimate the Al composition more precisely, XRD reciprocal space mapping is necessary.

In addition, we conducted (0002) (symmetric) and (10 $\bar{1}$ 2) (asymmetric) ω scans to estimate the densities of screw-type (Burgers vector length: 0.5185 nm (b_{screw})) and edge-type (Burgers vector length: 0.3189 nm (b_{edge})) threading dislocations, respectively (Figure S2)^{25,28,29}. Based on the FWHM of (0002) (symmetric) and (10 $\bar{1}$ 2) (asymmetric) ω scans (i.e. $\beta_{(0002)}$ and $\beta_{(10\bar{1}2)}$), screw- and edge-type threading dislocation densities (D_{screw} and D_{edge}) are estimated via^{25,28,29}:

$$D_{\text{screw}} = \frac{\beta_{(0002)}^2}{4.35b_{\text{screw}}^2}, \quad (3)$$

$$D_{\text{edge}} = \frac{\beta_{(10\bar{1}2)}^2 - \beta_{(0002)}^2}{4.35b_{\text{edge}}^2} \quad (4)$$

and tabulated in Table 1. Our XRD analysis suggests that sample A and C have similar amount of pure-edge- and screw-type threading dislocation densities.

X-ray diffraction reciprocal space mappings of (0002) and (10 $\bar{1}$ 5) planes (Fig. 5) are performed to quantify the (Al)GaN layers' strain and stress; in addition, the Al composition can be more precisely quantified compared to the $\omega/2\theta$ scan. Lattice constants a and c of each layer (GaN, Al $_x$ Ga $_{1-x}$ N, AlN) are obtained from Fig. 5 via the equation:

$$\left(\frac{1}{d_{hkl}}\right)^2 = \frac{4}{3} \left(\frac{h^2 + hk + k^2}{a^2}\right) + \frac{l^2}{c^2}, \quad (5)$$

where d_{hkl} represents the interplanar spacing of the probed lattice plane (hkl)³⁰. Employing the Poisson-Vegard's law³⁰ while including the lattice constant bowing parameter³¹, the Al composition (x), the free-standing lattice constants ($a_0(x)$ and $c_0(x)$), and the in-plane (ε_{xx}) and out-of-plane strain (ε_{zz}) of each layer are calculated via:

$$\begin{cases} \frac{c_m(x) - c_0(x)}{c_0(x)} = -\frac{2\nu(x)}{1 - \nu(x)} \times \frac{a_m(x) - a_0(x)}{a_0(x)} \\ c_0(x) = xc_{\text{AlN}} + (1 - x)c_{\text{GaN}} + \delta_c \cdot x \cdot (1 - x) \\ a_0(x) = xa_{\text{AlN}} + (1 - x)a_{\text{GaN}} + \delta_a \cdot x \cdot (1 - x) \\ \nu_0(x) = x\nu_{\text{AlN}} + (1 - x)\nu_{\text{GaN}}, \end{cases} \quad (6)$$

$$\varepsilon_{xx} = [a_m(x) - a_0(x)]/a_0(x), \quad (7)$$

$$\varepsilon_{zz} = [c_m(x) - c_0(x)]/c_0(x) \quad (8)$$

$a_m(x)$ and $c_m(x)$ are the measured lattice constants obtained from Eq. 5; $a_{\text{AlN}} = 3.112 \text{ \AA}$, $c_{\text{AlN}} = 4.982 \text{ \AA}$, $a_{\text{GaN}} = 3.186 \text{ \AA}$, and $c_{\text{AlN}} = 5.186 \text{ \AA}$, representing free-standing lattice constants. The Poisson ratio ν_{AlN} and ν_{GaN} are 0.203 and 0.183, respectively³⁰. δ_c and δ_a represent the deviation (bowing) parameter and were fit to be -0.036 and 0.018 \AA , respectively³¹. The in-plane stress (σ_{xx}) is also calculated according to:

$$\sigma_{xx} = [(C_{11} + C_{12}) - 2C_{13}^2/C_{33}] \times \varepsilon_{xx}, \quad (9)$$

where C_{ij} are the elastic constants of GaN ($C_{11} = 390 \text{ GPa}$, $C_{12} = 145 \text{ GPa}$, $C_{13} = 106 \text{ GPa}$, and $C_{33} = 398 \text{ GPa}$)³². The resulting in-plane stress values of GaN layers are tabulated in Table 1. Detailed XRD RSM calculation results,

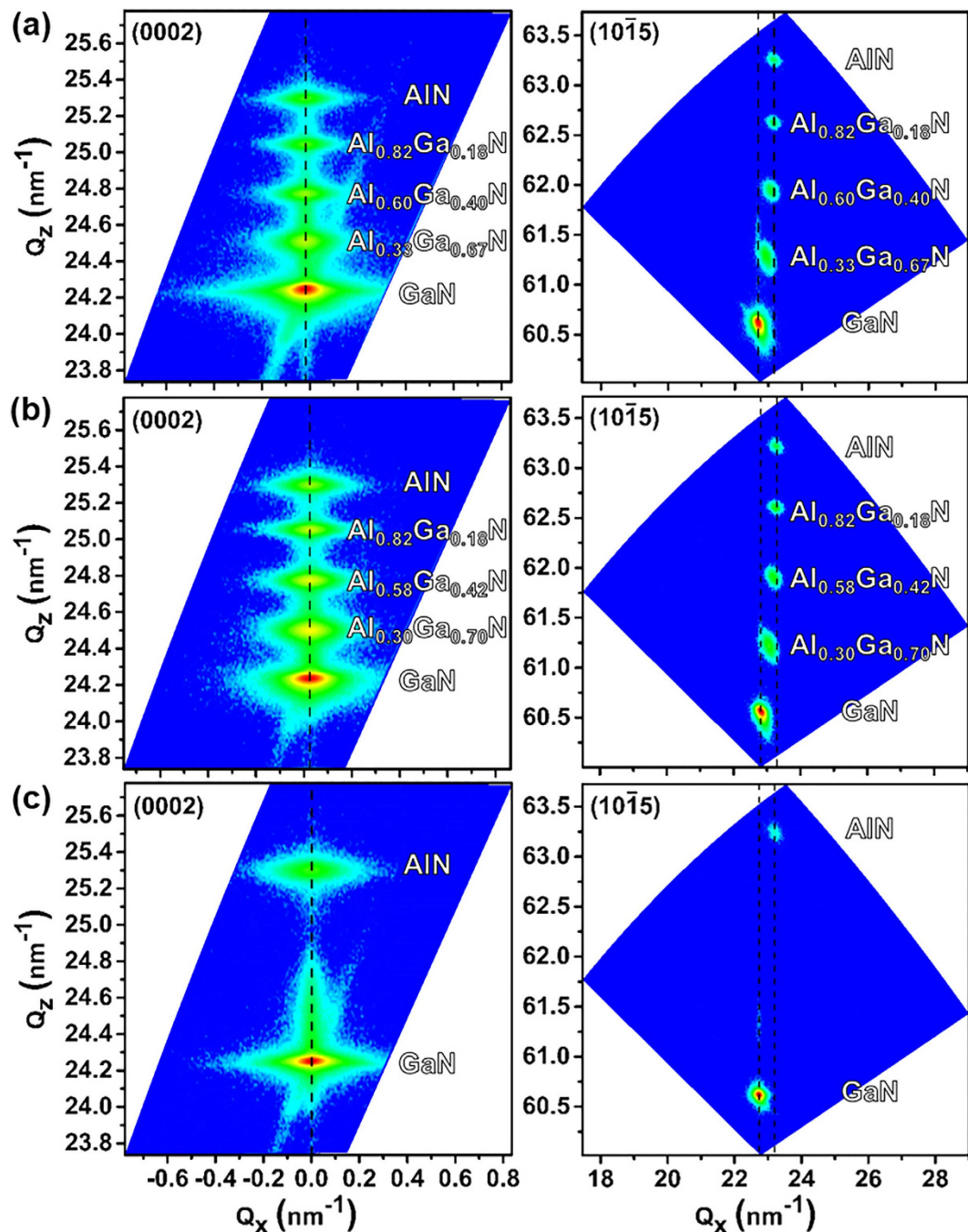


Figure 5. XRD reciprocal space mapping results reveal that the GaN layers of all samples (A, B, C) are under tensile strain along the c -plane and are under compressive strain normal to the c -plane. Amongst, sample B is observed to have the lowest GaN in-plane stress (Table 1).

including the lattice constants (a and c), in-plane strain/stress, and out-of-plane strain of each (Al)Ga $_x$ N layer in all samples, are provided in Supplementary Table S1. The in-plane strain of each (Al)Ga $_x$ N layer of the three samples are also plotted in Supplementary Figure S3. For sample A and B, from the AlN layer toward the Al $_x$ Ga $_{1-x}$ N layers the in-plane strain first decreases from positive (tensile), crossing the zero line (strain-free), and then become negative (compressive). Finally the in-plane strain returns to positive (tensile) due to the growing of the GaN layer. This discovered trend agrees with a previous work³³ where the in-plane strain in a GaN/Al $_x$ Ga $_{1-x}$ N/AlN system initially decreases along the increasing of the structure thickness and then crosses the zero line; as the thickness of GaN gets thicker the slope gets less steep, suggesting that an in-plane strain with a tensile component launches and becomes more dominant as the GaN thickness gets thicker.

Our XRD RSM results suggest that the GaN layers of all the three samples have tensile stress with sample B having the lowest stress (~ 0.154 GPa), sample C having the highest one (~ 1.548 GPa), and sample A having a medium value (~ 1.059 GPa). This indicates that the step-graded Al $_x$ Ga $_{1-x}$ N layers used in samples A and B reduce

the in-plane (tensile) stress of the GaN layer. Moreover, GaN in sample A is shown to have a higher in-plane tensile stress than GaN in sample B. We attribute this to sample A having a thicker GaN layer (a thicker i-GaN layer and an additional n-GaN layer) than sample B. Moreover, it's been reported that smaller-sized dopants, such as Si, in GaN films will form impurity atmospheres that limit the dislocation movement while growing, which further limits the dislocation reduction and the relief of the GaN tensile stress³⁴. At this stage, we fairly believe that the carbon dopant in the n-doped GaN in sample A has an equivalent effect on enlarging the GaN film tensile stress. This indicates the importance of optimal buffer layer configuration in terms of thicknesses and Al-content.

Investigation of the two dimensional electron gas characteristics via Hall effect measurement.

Hall effect measurements under Van der Pauw configuration are carried out at room (300 K) and low (77 K) temperatures. The metal contacts are formed via e-beam evaporation of 200-nm-thick Ti/200-nm-thick Ni metal stack and annealed at 750 °C under N₂ for 45 seconds. Samples are then diced into 5 mm × 5 mm squares and measured under Van der Pauw configuration.

Carrier concentration (N_s), sheet resistance (R_s), and mobility (μ_n) of samples A, B, and C are tabulated in Table 1. The 2DEG concentration is the highest in sample A, whereas 2DEG mobility is highest in sample B. It is earlier reported that carrier concentration and mobility of a 2DEG system are strongly related³⁵. At high 2DEG carrier concentration ($> 2 \times 10^{12} \text{ cm}^{-3}$), the 2DEG mobility has a negative dependence on increasing carrier concentration due to the surface roughness scattering, in agreement with our work. At low temperature (77 K), the 2DEG mobility increases and the sheet resistance decreases in all samples due to the reduced phonon scattering at low (77 K) temperature. Furthermore, 2DEG concentrations in all our samples are higher at 77 K than at 300 K, in line with other works³⁶.

Discussion

Our defectivity measurements via AFM and CL reveal that threading dislocation density reduces with increasing total buffer thickness. We further show step-graded AlGa_xN buffer layers and thicker GaN buffer layers alone are beneficial in doing so. This is attributed to the interaction of edge- and mixed-type threading dislocations in the forms of fusion (i.e. two threading dislocation lines merging into one) and annihilation (two threading dislocation lines (having opposite Burgers vectors) annihilating one another)¹⁴. As the (Al)Ga_xN film is further deposited, the possibility of such interactions increases, lowering the threading dislocation density. In particular, the inaccuracy of CL and XRD defectivity measurements are discussed here. As mentioned, CL measurement tend to underestimate the defectivity because these defects act as non-radiative recombination centers that possess capture radius; compared to AFM defectivity the lower defectivity of CL suggests that multiple defects are located within one CL dark capture radius. On the other hand, the estimated XRD defectivity here provides information about the densities of the pure-screw- and pure-edge-type threading dislocations; mixed-type threading dislocation, which typically occupies a large portion of the total defectivity, is not evaluated. In addition, although we conduct asymmetric rocking curve scan on the commonly used (10 $\bar{1}2$) plane to estimate the pure-edge-type threading dislocations, the measured XRD rocking curve FWHM is not solely affected by threading dislocations; other factors such as instrumental broadening, microstrain, and wafer curvature also play roles in changing the FWHM²⁵. We suggest to take the AFM defectivity as the total defectivity as it is the most direct and sensitive one, which concludes that sample C should possess a large amount of mixed-type threading dislocations that achieves its largest total defectivity.

X-ray diffraction RSM is used to investigate strain distribution in buffer layers (Fig. 5) providing in-/out-of-plane strain information of GaN, Al_xGa_{1-x}N, and AlN layers (Table S1). In samples A, B and C, the AlN in-plane tensile strain are found to be 0.47%, 0.51%, and 0.52%, respectively. We observe a gradual reduction of in-/out-of-plane tensile strain in the step-graded $3 \times \{\text{Al}_x\text{Ga}_{1-x}\text{N}\}$ buffer layers from Si(111) towards the AlGa_xN/GaN HEMT structure (Table S1 and Figure S3). This leads to a lower tensile GaN in-plane strain in samples A (0.23%) and B (0.03%) than that in sample C (0.34%), showing the importance of step-graded Al_xGa_{1-x}N buffer layers. Between sample A and B, GaN in-plane tensile strain in sample B is lower than that in sample A leading to a narrower XRD FWHM (Fig. 4). Although Raman spectroscopy reveals a blue shift of GaN E₂^H Raman peak in all samples, which corresponds to an in-plane compressive stress (<0.5 GPa), in line with other Raman works¹¹. The discrepancy between the stress results from XRD RSM and Raman spectroscopy has been found in previous works^{37,38}, which is suggested to be attributed to the fact that the stress measured by XRD RSM is an average value throughout the whole structure where the effect brought by local/random lattice distortion and/or any other imperfections are averaged out. On the other hand, the stress investigated by Raman spectroscopy is only from the spot-size area, therefore the value is statistically insufficient and less accurate to represent the strain in the whole GaN layer. In addition, it is reported that the discrepancy will also occur when the material is doped and/or with impurities³⁷. Furthermore, stress investigation using Raman Spectroscopy requires a phonon-shift estimation model, which might need to be modified for short period hetero-interfaces such as AlGa_xN/GaN HEMTs. Thus, we believe XRD RSM to be a more reliable means of probing the stress in thick hetero-interfaces than Raman studies.

Hall effect measurements under Van der Pauw configuration are carried out to determine 2DEG concentration, sheet resistance, and 2DEG mobility (Table 1). Sheet resistance is inversely related to the 2DEG mobility, however the relatively large variation of the sheet resistance of sample A and C should be attributed to the surface variation across the samples as the surface morphology is significantly affected by defects. As the defect density and type is varied, it is typical to have a varying surface morphology, and such variation in surface morphology greatly affects the contacts as defects are charged as well as some defects have threading component (during annealing metal is diffused further). The 2DEG concentration is the highest in sample A and the lowest in sample B whereas the 2DEG mobility is the highest in sample B and the lowest in sample A, showing a trade-off between 2DEG concentration and 2DEG mobility³⁵. Considering that sample A has the lowest threading dislocations but

sample B has the lowest in-plane strain, our work suggests that 2DEG mobility is not only affected by threading dislocations but also by GaN in-plane strain. As 2DEG concentration is affected by the spontaneous (P_{SP}) and piezoelectric (P_{PE}) polarizations in the $Al_xGa_{1-x}N$ barrier layer and the underlying GaN layer (where the piezoelectric polarization is determined by strain⁸), a fixed polarization charge density (C/m^2) is induced at the AlGaN/GaN hetero-interface given by:

$$\begin{aligned}\sigma(P_{SP} + P_{PE}) &= P(\text{GaN}) - P(\text{Al}_x\text{Ga}_{1-x}\text{N}) \\ &= \{P_{PE}(\text{GaN}) - P_{PE}(\text{Al}_x\text{Ga}_{1-x}\text{N})\} \\ &+ \{P_{SP}(\text{GaN}) - P_{SP}(\text{Al}_x\text{Ga}_{1-x}\text{N})\},\end{aligned}\quad (10)$$

where P_{SP} doesn't change with strain whereas P_{PE} follows:

$$P_{PE} = 2 \frac{a - a_0}{a_0} \left(e_{31} - e_{33} \frac{C_{13}}{C_{33}} \right).\quad (11)$$

where (C_{13} , C_{33}) are elastic constants and (e_{31} , e_{33}) are piezoelectric coefficients. For P_{PE} (GaN), $a_0 = 3.186 \text{ \AA}$, $e_{31} = -0.49 \text{ C/m}^2$, $e_{33} = 0.73 \text{ C/m}^2$, $C_{13} = 103 \text{ GPa}$, and $C_{33} = 405 \text{ GPa}$; for $P_{PE}(\text{Al}_x\text{Ga}_{1-x}\text{N})$, $x = 0.25, 0.23$, and 0.22 in sample A, B, and C, respectively), $a_0 \cong 3.165 \text{ \AA}$, $e_{31} \cong -0.52 \text{ C/m}^2$, $e_{33} \cong 0.92 \text{ C/m}^2$, $C_{13} \cong 104.25 \text{ GPa}$, and $C_{33} \cong 397 \text{ GPa}$ ⁸. Since the $Al_xGa_{1-x}N$ barrier layer is thin ($\sim 17 \text{ nm}$), we fairly assume that it is fully strained with no relaxation, which allows us to further assume that the lattice constant a of the $Al_xGa_{1-x}N$ barrier layer should be the same with that of the GaN layer. From Eqn. 11, we obtain: $P_{PE}(\text{GaN}) - P_{PE}(\text{Al}_x\text{Ga}_{1-x}\text{N}) \cong 0.057a - 0.172$, suggesting that as lattice constant a becomes larger (meaning that both the $Al_xGa_{1-x}N$ barrier and GaN layers simultaneously stretch further under more tensile strain), $\{P_{PE}(\text{GaN}) - P_{PE}(\text{Al}_x\text{Ga}_{1-x}\text{N})\}$ value and hence the polarization charge density (σ) increase. The increase in the polarization charge density results in an increase in 2DEG concentration, in good agreement with our observations. As stated before, the higher 2DEG concentration of sample A and C (due to their larger GaN tensile stress) is responsible for their lower 2DEG mobility because of the severer surface roughness scattering. In summary, we report that GaN layer in-plane tensile strain is the dominant mechanism governing the 2DEG characteristics.

Conclusion

Scanning electron microscopy, energy-dispersive X-ray spectroscopy, high resolution-cross section transmission electron microscopy, optical microscopy, atomic-force microscopy, cathodoluminescence, Raman spectroscopy, X-ray diffraction ($\omega/2\theta$ scan, symmetric/asymmetric ω scan (rocking curve scan), and reciprocal space mapping), and Hall effect measurements are utilized to investigate AlGaN/GaN HEMT structures on Si(111) with different buffer layer configurations. We show that thicker buffer layers are beneficial for reducing the threading dislocation density, and stacked $Al_xGa_{1-x}N$ buffer layers are critical for reducing the layer stress. Furthermore, our work suggests that the type and the magnitude of in-plane strain of the GaN layer, not the threading dislocation density, dominate the 2DEG mobility. Overall, we demonstrate the importance of optimal buffer layer configurations for 2DEG characteristics, which might allow high-frequency AlGaN/GaN HEMT designs on Si(111) substrates.

Methods

Sample preparation and cleaning. The AlGaN/GaN heterostructures used for this investigation are cut from three different 200-mm-diameter wafers (A, B, and C) with Si(111) substrate. The epitaxy layer configurations are shown in Fig. 1. Samples (8 pieces of sample A from the wafer A, 18 pieces of sample B from the wafer B, and 6 pieces of sample C from the wafer C) populate on the wafer approximately $\sim 15 \text{ cm}$ away from the center. Sample cleaning is carried out as follows: Samples are soaked in (1) hot trichloroethylene (TCE), (2) hot acetone, (3) hot methanol followed by (4) DI rinse and (5) N_2 blow dry. For steps (1–3), an ultrasonic bath cleaning is added. All steps are carried out for ~ 10 minutes.

Metallization, annealing, and dicing of AlGaN/GaN HEMT structures for Hall measurements.

After sample cleaning, 200-nm titanium (Ti) and then 200-nm nickel (Ni) metal contacts were deposited through a square-shaped patterned hard mask on the Hall mobility measurement samples. The metal deposition rates were kept between 1.5 and 2.0 $\text{\AA}/\text{s}$. Rapid thermal annealing was carried out at 750 $^\circ\text{C}$ for 45 s under N_2 for ohmic contact formation. Then, photoresist (PR) (AZ 5214) was spun on the samples then soft-baked at 95 $^\circ\text{C}$ for ~ 10 min in order to prevent scratching or damaging the sample surface during dicing. Finally, nickel-bond dicing blade (0.051 mm thick, 3–6 micron diamond grain size) mounted on K&S 708 dicing saw is used for dicing samples into small square dies with metal contacts in the four corners. Samples were re-cleaned before measurements. Hall measurement were performed three times for each piece of sample. Finally we calculate the overall averages and standard deviations of the measured data from these three kinds of samples.

References

- Pengelly, R. S., Wood, S. M., Milligan, J. W., Sheppard, S. T. & Pribble, W. L. A Review of GaN on SiC High Electron-Mobility Power Transistors and MMICs. *IEEE Trans. Microw. Theory Tech.* **60**, 1764 (2012).
- Ishida, M., Ueda, T., Tanaka, T. & Ueda, D. GaN on Si Technologies for Power Switching Devices. *IEEE Trans. Electron Dev.* **60**, 3053 (2013).
- Baliga, B. J. Gallium nitride devices for power electronic applications. *Semicond. Sci. Technol.* **28**, 074011 (2013).
- Kukushkin, S. A. *et al.* Substrate for epitaxy of gallium nitride: new material and techniques. *Rev. Adv. Mater. Sci.* **17**, 1 (2008).
- Dadgar, A. *et al.* Metalorganic Chemical Vapor Phase Epitaxy of Crack-Free GaN on Si(111) Exceeding 1 μm in Thickness. *Jpn. J. Appl. Phys.* **39**, L 1183 (2000).
- Krost, A. & Dadgar, A. GaN-Based Devices on Si. *Phys. Stat. Sol. (a)* **194**, 361 (2002).

7. Able, A., Wegscheider, W., Engl, K. & Zweck, J. Growth of crack-free GaN on Si(111) with graded AlGaIn buffer layers. *J. Cryst. Growth*. **276**, 415 (2005).
8. Ambacher, O. *et al.* Two dimensional electron gases induced by spontaneous and piezoelectric polarization in undoped and doped AlGaIn/GaN heterostructures. *J. Appl. Phys.* **87**, 334 (2000).
9. Saito, W. *et al.* High Breakdown Voltage AlGaIn–GaN Power-HEMT Design and High Current Density Switching Behavior. *IEEE Trans. Electron Dev.* **50**, 2528 (2003).
10. Trew, R. J. High-frequency solid-state electronic devices. *IEEE Trans. Electron Dev.* **52**, 638 (2005).
11. Cheng, J. *et al.* Growth of high quality and uniformity AlGaIn/GaN heterostructures on Si substrates using a single AlGaIn layer with low Al composition. *Sci. Rep.* **6**, 23020 (2016).
12. Miyoshi, M., Watanabe, A. & Egawa T. Modeling of the wafer bow in GaN-on-Si epiwafers employing GaN/AlN multilayer buffer structure. *Semicond. Sci. Technol.* **31**, 105016 (2016).
13. Arslan, E. *et al.* Buffer optimization for crack-free GaN epitaxial layers grown on Si(111) substrate by MOCVD. *J. Phys. D: Appl. Phys.* **41**, 155317 (2008).
14. Zhu, D., Wallis, D. J. & Humphreys, C. J. Prospects of III-nitride optoelectronics grown on Si. *Rep. Prog. Phys.* **76**, 106501 (2013).
15. Makaram, P., Joh, J., del Alamo, Jesús A., Palacios, T. & Thompson, C. V. Evolution of structural defects associated with electrical degradation in AlGaIn/GaN high electron mobility transistors. *Appl. Phys. Lett.* **96**, 233509 (2010).
16. Lee, S. R. *et al.* *In situ* measurements of the critical thickness for strain relaxation in AlGaIn/GaN heterostructures. *Appl. Phys. Lett.* **85**, 6164 (2004).
17. Kanaya, K. & Okayama, S. Penetration and energy-loss theory of electrons in solid targets. *J. Phys. D: Appl. Phys.* **5**, 43 (1972).
18. Takahashi, K., Yoshikawa, A. & Sandhu, A. *Wide Bandgap Semiconductors - Fundamental Properties and Modern Photonic and Electronic Devices* (Springer-Verlag, Berlin Heidelberg, 2007).
19. Nanjo, T. *et al.* Enhancement of Drain Current by an AlN Spacer Layer Insertion in AlGaIn/GaN High-Electron-Mobility Transistors with Si-Ion-Implanted Source/Drain Contacts. *Jpn. J. Appl. Phys.* **50**, 064101 (2011).
20. Wosko, M., Paszkiewicz, B., Paszkiewicz, R. & Tlaczala, M. Influence of AlN spacer on the properties of AlGaIn/AlN/GaN heterostructures. *Opt. Appl.* **43**, 61 (2013).
21. Bayram, C., Pau, J. L., McClintock, R. & Razeghi, M. Comprehensive study of blue and green multi-quantum-well light-emitting diodes grown on conventional and lateral epitaxial overgrowth GaN. *Appl Phys B* **95**, 307 (2009).
22. Mathis, S. K. *et al.* Modeling of threading dislocation reduction in growing GaN layers. *J. Cryst. Growth*. **231**, 371 (2001).
23. Speck, J. S., Brewer, M. A., Beltz, G., Romanov, A. E. & Pompe, W. Scaling laws for the reduction of threading dislocation densities in homogeneous buffer layers. *J. Appl. Phys.* **80**, 3808 (1996).
24. Rosner, S. J., Carr, E. C., Ludowise, M. J., Girolami, G. & Erikson, H. I. Correlation of cathodoluminescence inhomogeneity with microstructural defects in epitaxial GaN grown by metalorganic chemical-vapor deposition. *Appl. Phys. Lett.* **70**, 420 (1997).
25. Moram, M. A. & Vickers, M. E. X-ray diffraction of III-nitrides. *Rep. Prog. Phys.* **72**, 036502 (2009).
26. Sardela, M. R. Jr. *Practical Materials Characterization 10–12* (Springer, New York, 2014).
27. Denton, A. R. & Ashcroft, N. W. Vegard's law. *Phys. Rev. A* **43**, 3161 (1991).
28. Shan, L. *et al.* Super-aligned carbon nanotubes patterned sapphire substrate to improve quantum efficiency of InGaIn/GaN light-emitting diodes. *Optics Express* **23**, A957 (2015).
29. Wong, Y.-Y. *et al.* The effect of AlN buffer growth parameters on the defect structure of GaN grown on sapphire by plasma-assisted molecular beam epitaxy. *J. Cryst. Growth*. **311**, 1487 (2009).
30. Kadir, A., Huang, C.-C., Lee, K. E.-K., Fitzgerald, E. A. & Chua, S.-J. Determination of alloy composition and strain in multiple AlGaIn buffer layers in GaN/Si system. *Appl. Phys. Lett.* **105**, 232113 (2014).
31. Liou, B.-T., Yen, S.-H. & Kuo, Y.-K., Vegard's law deviation in band gaps and bowing parameters of the wurtzite III-nitride ternary alloys. Proc. SPIE 5628, Semiconductor Lasers and Applications II, (20 January 2005).
32. Kuball, M. Raman spectroscopy of GaN, AlGaIn and AlN for process and growth monitoring/control. *Surf. Interface Anal.* **31**, 987 (2001).
33. Mohan, N., Manikant, Soman, R. & Raghavan, S. Integrating AlGaIn/GaN high electron mobility transistor with Si: A comparative study of integration schemes. *J. Appl. Phys.* **118**, 135302 (2015).
34. Moram, M. A. *et al.* The effects of Si doping on dislocation movement and tensile stress in GaN films. *J. Appl. Phys.* **109**, 073509 (2011).
35. Katz, O., Horn, A., Bahir, G. & Salzman, J. Electron Mobility in an AlGaIn/GaN Two-Dimensional Electron Gas I—Carrier Concentration Dependent Mobility. *IEEE Trans. Electron Dev.* **50**, 2002 (2003).
36. Acar S., Lisesivdin S. B., Kasap M., Özçelik S. & Özbay E., Determination of two-dimensional electron and hole gas carriers in AlGaIn/GaN/AlN heterostructures grown by Metal Organic Chemical Vapor Deposition. *Thin Solid Films* **516**, 2041 (2008).
37. Ferreira, N. G., Abramof, E., Corat, E. J. & Trava-Airoldi, V. J. Residual stresses and crystalline quality of heavily boron-doped diamond films analyzed by micro-Raman spectroscopy and X-ray diffraction. *Carbon* **41**, 1301 (2003).
38. Liu, J. *et al.* Unintentionally doped high resistivity GaN layers with an InGaIn interlayer grown by MOCVD. *RSC Adv.* **6**, 60068 (2016).

Acknowledgements

This work was partially supported by the Air Force Office of Scientific Research (AFOSR) through Young Investigator Program Grant FA9550-16-1-0224 and was carried out in the Micro and Nanotechnology Laboratory and Frederick Seitz Materials Research Laboratory Central Facilities, University of Illinois at Urbana-Champaign, IL, USA. The authors acknowledge support from Dr. Mauro Sardela and Dr. James Mabon from Frederick Seitz Materials Research Laboratory. L. D. Rosario acknowledges financial support by the National Science Foundation under grant #NSF EEC-1359454 REU, as part of the nano@illinois project, managed and coordinated through the Center for Nanoscale Science and Technology collaboratory and the Micro and Nanotechnology Lab at the University of Illinois at Urbana-Champaign, IL, USA.

Author Contributions

C.B. conceived the idea and performed the epitaxial growth. H.-P.L. and C.B. designed the experiments. H.-P.L., J.P. and L.D. R performed fabrication/characterization of all samples. H.-P.L. and C.B. wrote the manuscript. H.-P.L. performed optical microscopy, SEM, EDX, AFM, XRD and Raman measurements. H.-P.L., J.P., and L.D.R carried out Hall measurements. H.-P.L. and C.B. participated in data analysis. All authors discussed the results and commented on the manuscript.

Additional Information

Supplementary information accompanies this paper at <http://www.nature.com/srep>

Competing financial interests: The authors declare no competing financial interests.

How to cite this article: Lee, H.-P. *et al.* Investigation of AlGa_N/Ga_N high electron mobility transistor structures on 200-mm silicon (111) substrates employing different buffer layer configurations. *Sci. Rep.* **6**, 37588; doi: 10.1038/srep37588 (2016).

Publisher's note: Springer Nature remains neutral with regard to jurisdictional claims in published maps and institutional affiliations.



This work is licensed under a Creative Commons Attribution 4.0 International License. The images or other third party material in this article are included in the article's Creative Commons license, unless indicated otherwise in the credit line; if the material is not included under the Creative Commons license, users will need to obtain permission from the license holder to reproduce the material. To view a copy of this license, visit <http://creativecommons.org/licenses/by/4.0/>

© The Author(s) 2016